Quantitative thermoelastic stress analysis by means of low-cost setups

Published in:
Optics and Lasers in Engineering

Document Version:
Peer reviewed version

Queen's University Belfast - Research Portal:
Link to publication record in Queen's University Belfast Research Portal

Quantitative Thermoelastic Stress Analysis by means of low-cost setups

Giuseppe Pitarresi[1,*], Riccardo Cappello[1] and Giuseppe Catalanotti[2]

[1] *Dipartimento di Ingegneria (DING) - Università degli Studi di Palermo, Viale delle Scienze Ed. 8, 90128 Palermo, Italy*

[2] *Advanced Composites Research Group (ACRG), School of Mechanical and Aerospace Engineering, Queen's University Belfast, Belfast BT9 5AH, UK*

Abstract

A low-cost Thermoelastic Stress Analysis (TSA) experimental setup is proposed which uses an ordinary micro-bolometer and in-house developed signal processing scripts. The setup is evaluated by analysing the thermoelastic signal from a tensile and a SENT specimen made of stainless steel AISI 304L, and the bolometer performances are compared with those of a state of the art photon detector. Signal processing is based on off-line cross-correlation, using a self-reference signal which is retrieved from the acquired thermal data. Procedures are in particular developed to recognise, quantify and correct errors due to spectral leakage and loss of streamed frames. The thermoelastic signal amplitude/phase, the thermoelastic constant and the Mode I Stress Intensity Factor (SIF) from the bolometer and photonic cameras are evaluated considering the influence of loading frequency, sampling frequency, detector array sub-windowing and acquisition interval duration. A camera-specific linear calibration procedure is applied to correct the thermoelastic signal obtained with the bolometer. The procedure is extended to correct also SIF values, finding a good match with the SIFs obtained by the photon detector. An automatic iterative algorithm, based on the least square fitting of Williams' series functions, is proposed to identify the crack tip position. An estimation of processing times of the developed signal processing scripts has been carried out, finding that a full crack characterisation (TSA maps, crack tip position, SIF) can be performed with a data acquisition time of 10-20 s, a post-processing time of less than 2 s and an overall hardware cost under 10 k€.

Keywords: Thermoelastic Stress Analysis; IR-Thermography; Micro-bolometers; Fatigue Testing; Crack-growth monitoring; Signal Processing.

** Corresponding author: giuseppe.pitarresi@unipa.it

1. Introduction

The present study investigates the possibility to perform quantitative Thermoelastic Stress Analysis by using a low-cost setup (below 10 k€). This is mainly achieved by using general-purpose micro-bolometer infrared cameras, in-house developed data-processing scripts, and setup-specific calibration procedures. Thermoelastic Stress Analysis (TSA) is the typical denomination given to a well-established experimental stress analysis technique, based on retrieving the temperature changes induced, in stressed materials, by the Thermoelastic Effect [1–3]. Isotropic materials stressed under linear elastic and adiabatic conditions, develop temperature variations, dT, that are linearly correlated to the sum of normal stresses, σ_{ii}. Therefore, evaluating such dT provides a full-field representation of the σ_{ii} stress metric. TSA is conveniently implemented under cyclic loading. This favours the onset of adiabatic conditions, and modulates the thermoelastic signal so that an effective suppression of noise can be achieved with band-pass frequency filtering and time-averaging cross-correlation [4,5]. When a sinusoidal load is applied, the thermoelastic-effect induced temperature change is coded as the amplitude of the harmonic of temperature at the load frequency. In this case, the resulting relationship allowing quantitative TSA writes:

$$\Delta T = -\, T_o C_{th} \Delta (\sigma_{xx} + \sigma_{yy}) \tag{1}$$

where ΔT and $\Delta \sigma_{ii}$ are, respectively, the temperature and stress changes produced by a peak-to-peak load change, C_{th} is the material *Thermoelastic Constant*, and T_o is the average absolute temperature.

Progresses in hardware and digital signal-processing have made possible the use of Focal Plane Array (FPA) infrared cameras and short processing times. For TSA, the overall measurement time comprises a first step of temperature collection, over a time-window of few tens of seconds, and a subsequent stage of data processing, which can be as short as 1 second. Therefore, TSA is a well suited technique for monitoring moderately fast-changing scenarios, such as those where cracks or defects evolve under the action of fatigue loadings. TSA can also provide information about the onset of dissipation of mechanical energy, which may cause phase-shifts and the rise of a second and higher harmonic components, whose evolutions can also provide indications for an early evaluation of some materials fatigue-life limits [6–10]. Other useful applications comprise: evaluation of fracture mechanics parameters [11,12], monitoring of cracks, delaminations and identification of

damaging sites [7,13–15], quantitative and qualitative Non-Destructive Testing and Structural Health Monitoring evaluations [13,16,17].

Since its first appearance in the mid-eighties, adoption of TSA has never declined, with examples of qualitative and quantitative applications regularly proposed, mostly regarding studies of the fatigue behaviour of materials and structures. Nevertheless, the know-how and interest towards TSA has remained confined to a rather few number of practitioners, and has seldom reached a broader mass of users, both in industry and academia. Two main reasons for such a limited diffusion can be identified: the high costs of cooled photon-detector IR-cameras, required for optimal temperature measurement, and a low awareness of the data-processing required. This is for instance witnessed by the rather limited number of works in the literature which have used in-house developed coding instead of less flexible and often camera-specific commercial solutions. Therefore, an increasing number of researchers is trying to investigate the possibility to adopt more affordable types of IR detectors and more flexible setups.

Some authors have investigated the implementation of TSA with mirror driven single-detector IR-scanners [18,19]. These works have also proposed off-line data processing schemes implemented in Matlab, which do not require reference load signals. The main limit of such setups is that they cannot perform full-field analyses, but remain interesting solutions for line-wise analyses [19]. In [20] a QWIP FPA photo-detector was used to perform full-field analyses, using the same Matlab based data processing of [18]. Rajic et al. [5,21] have investigated the adoption of low-cost and handier micro-bolometer sensors. They showed that cross-correlation is able to improve the signal-to-noise ratio beyond the Noise-Equivalent-Temperature-Difference (NETD) sensitivity of micro-bolometers. Moreover, TSA performed with micro-bolometers can achieve sensitivities to stress detection similar to those of photon detectors, and even better if the acquisition time window is extended in time. Some works have started to exploit these features, and have proposed portable and efficient setups for structural health and crack-growth monitoring applications [16,17,22,23].

An important drawback with micro-bolometers, which affects TSA accuracy in stresses evaluation, regards the signal attenuation and shifting determined by the different dynamic response of these sensors [21]. In particular, the quantitative response of micro-bolometers strongly depends on the loading frequency, and attenuation increases with an increase of such frequency [21,24,25]. Sampling frequency is instead expected to have a lower impact on accuracy, since the ability of cross-correlation to extract the signal amplitude should

be preserved as long as sampling is performed above the Nyquist frequency. This because cross-correlation is essentially equivalent to performing a Discrete Fourier Transform (DFT) [26].

In order to still perform TSA in a quantitative way, while exploiting the advantages of micro-bolometers, some authors have recently tried to model the dynamic response of such detectors to come out with correction calibration procedures. Rajic and Rowlands [21] proposed an analytical model to fit the frequency response of a Flir A20M system in terms of amplitude and phase. They showed how such model can be fully characterised by factory calibration experiments, thus remaining opaque to the user, while providing the necessary thermoelastic response corrections. A simpler approach was proposed by Jimenez-Fortunato et al. [25], who adopted a Flir A655sc camera and performed calibration tests on tensile samples, highlighting that the thermoelastic signal attenuation ratio is not dependent on the load amplitude applied. They proposed a semi-logarithmic law to model the influence of loading frequency, which could be used to correct the thermoelastic signal amplitude. Similarly to [21], the approach in [25] is based on characterising the load frequency response of the micro-bolometer with a preliminary and specific calibration procedure. The calibration procedure proposed in [21], was also applied to correct TSA maps from a Single Edge Notched Tension (SENT) specimen [23]. The bolometer data, though, were used only to automatically track the crack tip location, while the SIF calculation relied on analytical solutions available only for specific sample geometries.

Here, a methodology to measure the thermoelastic signal from temperature data acquired with any IR camera is proposed. This is based on both DFT and cross-correlation and is able to eliminate the influence of spectral leakage and frame dropping, which could result in errors higher than 35 % if not dealt with. The proposed data processing scheme was implemented in a Matlab script, and applied to data collected from Tensile and SENT steel samples, which were monitored simultaneously by a micro-bolometer camera Flir A655sc and a cooled-sensor camera Flir X6450sc. This has allowed to investigate and compare the influence, on the performance, of the two types of sensors, of a number of different experimental parameters (Load Amplitude, Load Frequency, Sampling Frequency and data collecting Time-Window). It is demonstrated that accurate quantitative stress analyses can be performed with micro-bolometers also at short Time-Windows. The proposed off-line signal processing is able to provide full data analyses in short time (< 2 s) including also features such as crack-tip tracking based on the stress maps. Finally, the ability of providing a quantitative

analysis (after a preliminary load-frequency calibration) was demonstrated showing that values of the Stress Intensity Factor obtained with both IR cameras are in excellent agreement.

2. Experimental Set-Up

2.1 Samples description

Two samples, a dog-bone shaped Tensile (T) and a Single Edge Notched Tension, were tested. Both samples are made of the same material: AISI 304L stainless steel, and their dimensions are reported I Fig. 1. The SENT sample has a crack of length about half the sample width, obtained by previous fatigue cycling. The front and rear faces of each sample were preliminary painted with matt black paint to enhance and uniform infrared emissivity.

The Tensile sample (hereinafter denotes as T) was chosen to investigate the different thermoelastic response and thermoelastic calibration behavior of the two IR-cameras. The average and standard deviation of the thermoelastic signal were calculated from a Region of Interest (ROI), and used to evaluate the thermoelastic constant C_{th} and the noise-to-signal ratio. The ROI is a rectangular area over the central region of the sample (see Fig. 1a).

The SENT sample (hereinafter denoted as S) was chosen to investigate the thermoelastic behavior in presence of biaxial stress states, strong stress gradients, and to evaluate the impact of signal attenuation in the micro-bolometer camera on the measured Stress Intensity Factor (see Section 3.3).
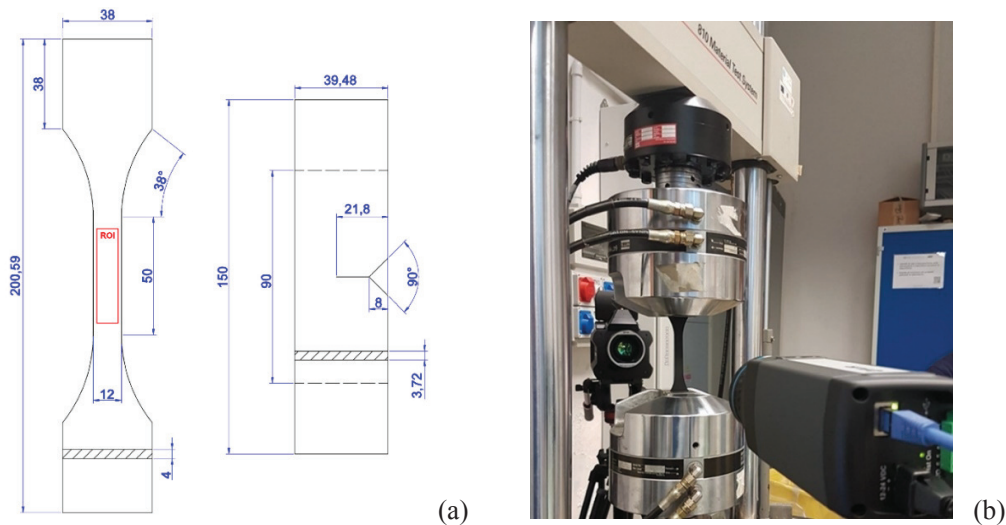

(a) (b)

Figure 1: a) drawings of the two tested samples; b) photo of the Tensile sample during a test, and position of the two IR cameras.

2.2   Hardware setup

Samples were loaded in a servo-hydraulic MTS 810 testing machine, equipped with MTS 647 hydraulic wedge grips. All tests were run in load control, by setting a sinusoid load mean, amplitude and frequency. Two Infrared cameras are used: a micro-bolometer Flir A655sc (from now on indicated as B) and a cooled InSb photon-detector Flir X6540sc (from now on indicated as P). Each IR camera stared at a different side of the sample, as shown in Fig. 1b. This allowed to simultaneously use the two IR cameras for each set of test parameters (see Section 2.3 and Fig. 2). During all tests the camera spatial resolution was kept constant, at 0.26 mm/pixel for the Tensile tests and B camera, 0.34 mm/pixel for the Tensile tests and P camera, 0.37 mm/pixel for the SENT tests and cameras B, 0.34 mm/pixel for the SENT tests and cameras P. In all tests, the *integration time* of the P camera was set at 659 µs.

Each acquisition was started after stabilization of the load cycle, and the acquisition Time-Window ranged between 60 and 120 s (see Fig. 2). Data streaming and storage was controlled by two PCs, one for each camera, by means of the software FLIR *ResearchIRmax v. 3.4*, which allowed to save the acquired sequence of thermograms in .mat files for further data processing in Matlab. In particular, the P camera was connected to a laptop PC (DELL XPS15) via the camera gigabit Ethernet port to the laptop USB-C port by means of an Ethernet to USB-type-c adapter. The B camera was connected via its gigabit Ethernet port to the RJ45 Ethernet port of the motherboard of a desktop PC.
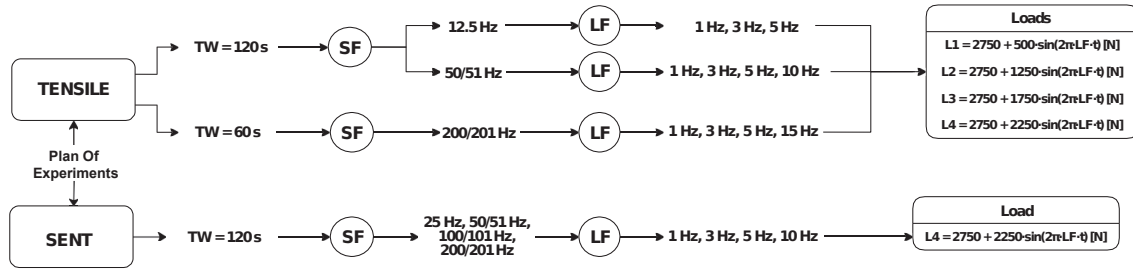
Figure 2: Summary of tests settings. Legend: TW – time window, SF – Sampling Frequency, LF – Loading Frequency, t – time, Lx – loading applied (x=1,2,3,4).

2.3   Plan of Experiments

Figure 2 summarizes all tests performed and the relative set parameters. All these tests were performed by both cameras B and P simultaneously, unless otherwise specified.

Tests on the T sample were performed at four increasing load amplitudes (all having the same mean value, see Fig. 2). Tests on the S sample were performed under pure mode I sinusoid loading, between 500÷5000 N (load

ratio R=0.1). This load range was verified to provide a very slow crack growth, so that variations in the crack length could be considered negligible throughout all the tests performed, keeping the nominal SIF value virtually constant.

Both samples, T and S, were tested with different Load Frequencies (LF), temperature sampling frequencies (SF), and acquisition time interval durations (TW).

While the P camera allowed to crop the area of signal acquisition around the sample (sub-windowing), the B camera has more limited and fixed sub-windowing options, therefore data acquired at frame rates of 12.5, 25 and 50 Hz used the sensor full field-of-view (FOV) of 640x480 pixels; data acquired at 100 Hz used a 640x240 pixels FOV; and data acquired at 200 Hz used a 640x120 pixels FOV. To allow the whole tensile sample to fill in the FOV also for the 200 Hz tests, the B camera was tilted by 90° (as shown in Fig. 1b), so that the wider size of 640 pixels was always aligned with the specimen axis.

In the next Sections each test, when needed, will be identified with an alphanumeric label which follows the sequence: (IR camera type)+(sampling frequency)+(sample type)+(loading frequency)+(applied load). Therefore, test B50T3L2 will indicate micro-bolometric data sampled at 50 Hz on the tensile sample loaded at 3 Hz with load amplitude L2=2750+1250·sin(2π·LF·t) [N].

3. Methodologies of signal processing

Data processing is performed with in-house developed Matlab scripts. An example of code used for the evaluation of the thermoelastic signal from collected thermal frames is reported in Appendix A. The thermograms, acquired as .seq or .ptw Flir formats, are exported into .mat files using the Flir ResearchIRmax software. Post-processing in Matlab consisted of two different phases. The first one performs the evaluation of the Thermoelastic Signal and includes two optimization procedures to mitigate errors due to the occasional loss of thermograms and errors due to spectral leakage. The second step processes the Thermoelastic Signal to retrieve the Thermoelastic Constant and the Mode I SIF, from the T and S samples, respectively.

3.1 Data processing for the evaluation of the Thermoelastic Signal

The implemented post-processing procedure consists of the following steps.

STEP 1 – recovery of frames continuity:

The regular time sequence of acquired thermograms is checked against the possible lack of frames (hereinafter referred to as frame-drop). In particular, this can arise whenever the signal is streamed to an external PC. The information about sampling timing can be obtained by importing from Flir ResearchIRmax a .csv file of the temperature data from a selected point in the thermograms. From the .csv it is retrieved the time at which each frame was acquired, from which it is straight forward to verify the presence and location of frame-drops. It was found that both IR cameras, P and B, have occasionally presented the occurrence of frame-drops, and a description and estimation of the error produced in the thermoelastic signal is reported in Section 4.1. It is reported also that the likelihood and severity of frame-drop increases with the increase of sampling frequency and with the type of data streaming. For instance, the giga-ethernet cable used in this work to connect the P camera to the laptop PC required an Ethernet RJ45-to-USB adapter. It was found that USB-C performs better than USB 3.0, while USB 2.0 can give rise to an elevated number of frame drops.

In order to restore the missing frames, a Matlab routine was run which built the required frames by averaging the frames immediately available before and after the empty positions. This provided an effective correction, as it was observed that restoring the correct time sequence is more important than recovering the exact temperature values that have been lost.

STEP 2 – evaluation of frequency content:

The frequency content can be analysed at a glance by performing the Discrete Fourier Transform of the time-temperature signal. This is done in Matlab by the Fast-Fourier Transform *fft* function. Figure 3 shows some examples of Power Spectrums, where the plotted amplitude is obtained by rescaling the *fft* output as follow:

$$abs(squeeze(fft(frames(row,column,1:N)))) ./N \qquad (2)$$

where Eq. (2) is in Matlab code, with N being the number of samples, "frames" a third-order tensor variable containing all frames (where the 3rd dimension is time, see also Appendix A and Fig. A1), and row and column indicates the coordinates of a point in the thermogram that is being evaluated. Equation (2) provides the amplitude for the DC term (i.e. at zero frequency), and needs to be multiplied by a factor 2 to yield the correct amplitude of harmonic terms.
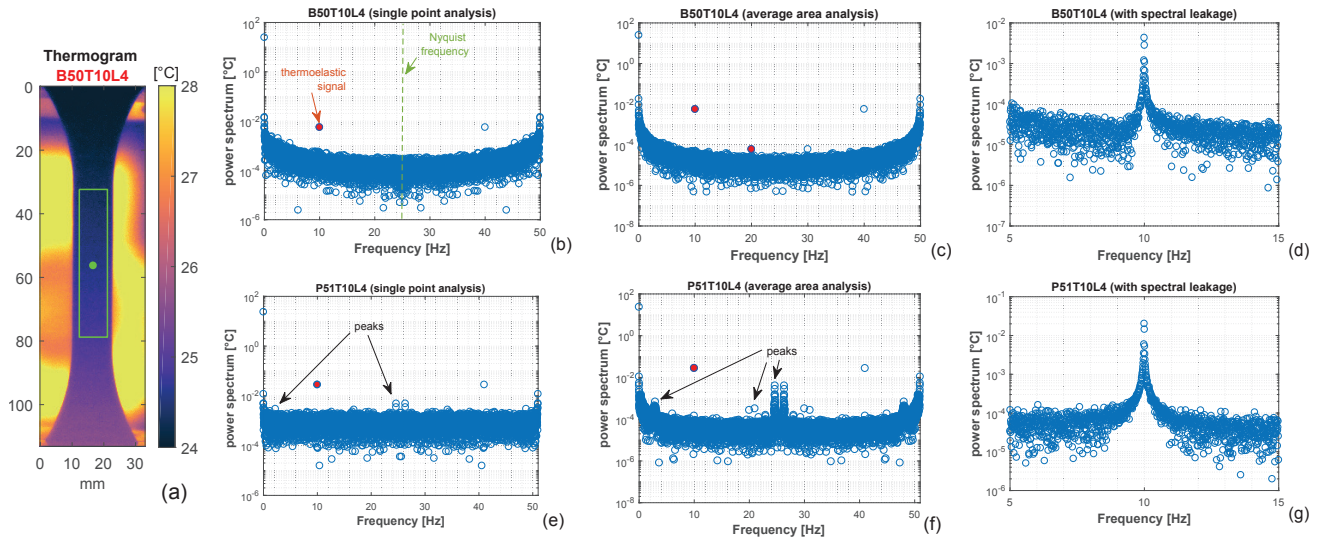
Figure 3: a) Image of a thermogram of a T sample with sith a point and area selected for DFT analysis; b÷g) DFT power spectrums from the microbolometer B (b,c,s) and photonic-detector P (e,f,g).

The power spectrum plots provide a number of useful information. First of all, it is observed that they are symmetric about the Nyquist frequency, equal to half the sampling frequency. In TSA, regardless of the filtering analysis used, the sampling frequency must be always higher than twice the loading frequency. This could pose a limitation to micro-bolometers, whose sampling rates usually top values around 60 Hz, which limits the max applicable load frequency to 30 Hz (15 Hz if the second-harmonic signal is also of interest). The power spectrum also provides information about the noise floor, and hence about the presence of other harmonics above it. These could arise in areas where there is a non-sinusoidal thermo-mechanical coupling or could be linked to aliasing or spectral leakage. The ideal situation is when the thermoelastic harmonic is well isolated at a single frequency value, and the nearby frequency bins present values within the noise floor (e.g. Fig. 3.b,c,e,f). It is also interesting to compare the level of noise floor between the B and P camera (Fig. 3). When a single point is analysed, the noise floor is comparable, and generally below 2 mK, i.e. about an order of magnitude below the cameras NETD, thanks to the random noise filtering operated by cross-correlation, as observed by Rajic et al. [5]. It is interesting to notice that the B camera presents a reduction of the noise floor as the frequency increases up the Nyquist value. The P camera, instead, has a flat noise floor, and presents some peaks which are not detected by the B camera (see Fig. 3f). Such peaks are not eliminated by averaging over the ROI, as shown comparing Fig. 3e and 3f, and are affected by leakage. Only a few works in the literature have reported similar whole-spectrum analyses, among which the works of Urbanek and Bar, [27,28], where similar peaks have been observed and explained as caused by aliasing or vibrations from the

testing rig. Figures 3c,f show the power spectrum of the average signal from the central rectangular area of the sample, marked in Fig. 3a. It is seen that the spatial averaging operation combined with the cross-correlation produces a further reduction of the noise floor in both P and B cameras, de-facto improving sensitivity. In Fig. 3c, for instance, the second harmonic signal, typically smaller than the thermoelastic signal, is now revealed as the noise floor has lowered. Some recent works have used the second harmonic signal amplitude as an effective thermos-mechanical parameter for the early detection of the material fatigue limit [6,9]. In these studies, a change of slope of the second harmonic versus the increasing value of $\Delta\sigma_{ii}$ is assumed to be correlated to the material fatigue limit. Such procedures would benefit from analysing the second harmonic of the spatially averaged thermal signal, as the above demonstrated increase in sensitivity would allow a better identification of the onset of a different rate of increase.

Another significant outcome from power spectrum plots is the possibility to recognise when the thermoelastic harmonic is affected by spectral leakage. In fact, whenever this happens, the thermoelastic harmonic peak shows a cusp like trend (see Figs. 3d,g), with surrounding frequency bins having amplitudes above the noise floor. Spectral leakage can produce a severe attenuation in the thermoelastic signal amplitude (see Section 4.1), and also an error in the evaluation of the frequency carrying the thermelastic signal, which is no longer coincident with the bin of the maximum local value of spectrum amplitude. Therefore, means for reducing spectral leakage are essential in TSA.

STEP 3 – suppression of spectral leakage:
Leakage is primarily introduced by the discrete nature of sampling [29]. Pitarresi [26] showed that leakage may equally affect all the common filtering procedures, i.e. Lock-In digital cross correlation, Least Square Fitting and Discrete Fourier Transform [26], and only a few authors have evidenced this potential problem in TSA [18,20,26,28]. In the case of a pure sinusoidal loading, spectral leakage is always present when the number of acquired and processed loading cycles is not an integer. Therefore, the solution proposed here to reduce leakage is to decrease the number of frames until the condition of an integer number of load cycles is approached or satisfied. Since TSA analyses generally deals with relatively high number of frames (typically above 1000), and since the suppression of a few frames is generally enough to reduce leakage (see also Section 4.1), the proposed solution is practical and easy to implement. This procedure has the effect of providing a frequency bin right at the value of the load frequency, and consequently the cusp-like trend in the power

spectrum collapse in a single peak (see again the comparison between Fig. 3b and 3d, and 3e and 3g). Two situations may arise when implementing the above-mentioned strategy of leakage suppression:

- The load frequency is not known or is affected by uncertainty: in this case the number of frames is progressively reduced until the power spectrum amplitude between the main local peak and the adjacent bins is maximized, which corresponds to the cases of Figs. 3c,f;

- The load frequency is known: in this case the number N of frames to cut off is that which makes the value of k an integer, where k is the bin number at the load frequency, defined as:

$$k = \text{LF} \cdot \frac{N}{SF} \tag{3}$$

Since (SF/N) is the fundamental frequency, Eq. (3) guarantees that LF takes an integer value of frequency domain units.

It is finally observed that if a cusp-like peak still remains after Eq. (3) is satisfied, this is very likely due to the presence of frame-drops in the processed sequence. Therefore STEP 1 always needs to be accomplished, and the visual spectrum analysis procedure is useful for detecting also the occurrence of frame losses.

STEP 4 – cross-correlation

Once the number of frames has been optimized to prevent leakage, one computationally simple way to obtain the thermoelastic signal amplitude and phase is by applying the two following equations giving the in-phase, X, and in-quadrature, Y, components of the thermoelastic signal [4,26,30]:

$$X = \frac{2}{N} \cdot \sum_{i=1}^{N} T_i \cdot \sin\left(\frac{2\pi}{N} k \cdot i\right); \quad Y = \frac{2}{N} \cdot \sum_{i=1}^{N} T_i \cdot \cos\left(\frac{2\pi}{N} k \cdot i\right) \tag{4}$$

$$\Delta T = \sqrt{X^2 + Y^2} \tag{5}$$

where k is the load frequency bin (or lock-in frequency), given by Eq. (3), and ΔT in Eq. (5) represents the peak-to-peak amplitude of the thermoelastic effect induced temperature change. In a similar way, it is possible to filter out the amplitude and phase of any harmonic of the spectrum, by just changing the value of k. For instance, using a frequency bin equal to $2k$ would yield the so called 2nd Harmonic [12].

It is observed that the same result of ΔT given by Eq. 5 could be obtained by just applying the command in Eq. (2) to each pixel of the selected region of analysis. At this regard, it is observed that Eqs. (4) are formally similar to the relationships defining the harmonic components of the DFT, and therefore the two routes are mathematically equivalent [26]. The convenience of using the DFT directly, is given when a software such as

Matlab is available, where the DFT is readily computed by the *Fast-Fourier-Transform* algorithm (*fft* command). Otherwise, Eqs. (4) are easier to implement with basic programming skills or software platforms (see Appendix A and Section 5.2 for further considerations about algorithms running times).

3.2   Evaluation of the Thermoelastic Constant

The thermoelastic constant C_{th} in Eq. (1) is obtained from the slope of the linear fitting of points $(\Delta T_{avg}, \Delta \sigma_{xx})_i$, where i indicates the load amplitude. Therefore, the linear fit is performed on four points, one per each applied load amplitude (see Fig. 2). ΔT_{avg} is the average amplitude of the thermoelastic signal, computed over the sample ROI shown in Fig. 3a, which comprises about 1500 pixels. $\Delta \sigma_{xx}$ is the theoretical axial stress variation. One linear fitting is performed for each set of LF and SF values (as reported in Fig. 2), and for each camera type, P and B. Values of C_{th}, Coefficient of Determination of the linear regression, R^2, and Standard Deviation, St.Dev., of the thermoelastic signal over the ROI are computed.

3.3   Evaluation of the Stress Intensity Factor

The Mode I SIF variation ΔK_I is evaluated from SENT tests by a *least-square fitting* of the experimental data with the analytical prediction of the Williams' series solution [12], which leads to the following tensor equation:

$$
\begin{bmatrix} \cdots \\ (\Delta T)_i \\ \cdots \end{bmatrix}_i = -T_o C_{th} \begin{bmatrix} \cdots & \cdots & \cdots & \cdots & \cdots & \cdots \\ \dfrac{1}{\sqrt{2\pi}\sqrt{r_i}}\cos\left(\dfrac{\vartheta_i}{2}\right) & 4 & \sqrt{r_i}\cos\left(\dfrac{\vartheta_i}{2}\right) & 8r_i\cos\vartheta_i & 10r_i\sqrt{r_i}\cos\left(\dfrac{3\vartheta_i}{2}\right) & \cdots \\ \cdots & \cdots & \cdots & \cdots & \cdots & \end{bmatrix}_{i \times n} \times \begin{bmatrix} \Delta A_{I1} = \Delta K_I \\ \Delta A_{I2} \\ \Delta A_{I3} \\ \Delta A_{I4} \\ \Delta A_{I5} \\ \cdots \end{bmatrix}_n \quad (6)
$$

In this work five terms of Williams' series function are used and the experimental data feeding Eq. (6) are taken from an annular section placed in front of the crack tip, having minimum and maximum radiuses of about 1.5 mm and 10.5 mm and an angular extension of 135° (see Fig. 4).
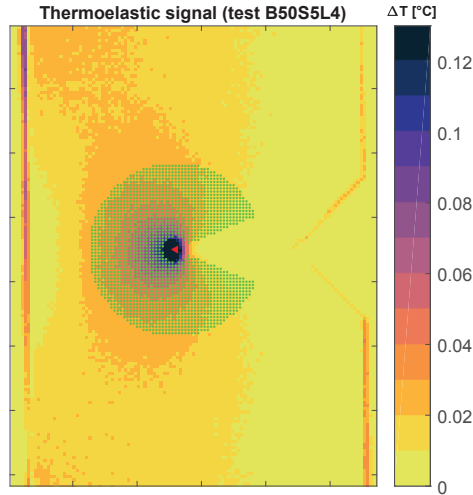
Figure 4: annular sector around the crack tip where points are taken to feed to the fitting model.

From Eq. (6) it is seen that the coefficients in the matrix depend on the polar coordinates of the points comprised in the annular area. Therefore, in order for the fitting to provide meaningful results, it is necessary to accurately estimate the position of the crack tip. In this work, the coordinates of the crack tip are taken as those of the centroid of the pixel which maximises the coefficient of determination R^2 ($0 \leq R^2 \leq 1$) of the fitting, defined as:

$$R^2 = 1 - \frac{RSS}{TSS} \tag{7}$$

where *RSS* and *TSS* are the Residual Sum of Squares and Total Sum of Squares [12]. In particular, an iterative procedure is implemented in Matlab, where an initial guess point is chosen, reasonably close to the crack tip (e.g. the pixel of maximum temperature within the sample), and the value of R^2 is then evaluated for each point belonging to a search area centered on the guess point. The iterative calculation yields the pixel with the maximum R^2, which is assumed to be the crack tip. An example is drafted in Fig. 5, where an initial guess point is chosen considerably far off from the crack tip, to verify the robustness of the search procedure.
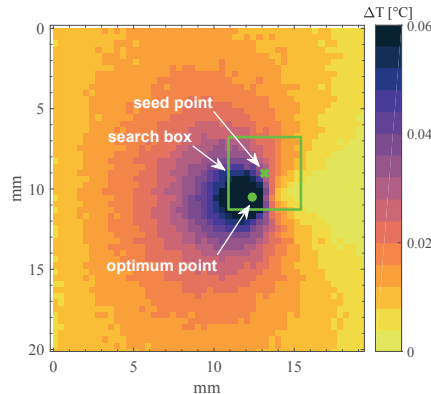

Figure 5: example of selection of the area of search of the crack tip.

4. Results and discussion #1: Tensile sample

In this section, values of ΔT, ΔT_{avg}, C_{th}, R^2 and $St.Dev.$ from the P and B camera are analyzed and compared. The comparison is carried out considering the influence of the following setting parameters: LF, SF and TW. One first outcome that is evidenced concerns the evaluation of ΔT versus $\Delta\sigma_{ii}$. Figure 6 provides an example from four tests, two with the B and two with the P camera, with different SF (200 Hz and 12.5 Hz) but equal LF (5 HZ). It is observed that the thermoelastic signal shows a very good linear correlation with the load amplitude, as foreseen by the Thermoelastic law (Eq. 1), and that the slope of the linear fit for the results from the B camera depends on the SF, while for the P camera is virtually unaffected and the two fits basically overlaps. It is reported that the R^2 value obtained from linear regression in all performed tests with the B camera and for all combinations of LF, SF and TW, has been found between $0.9996 < R^2 < 0.9999$. Therefore, it can be concluded that even if the micro-bolometer measured thermoelastic signal is attenuated, due to the dynamic response of the sensor, for a given SF, the ratio of attenuation with respect to the correct value (here assumed to coincide with that from the P camera) is constant with the load amplitude.
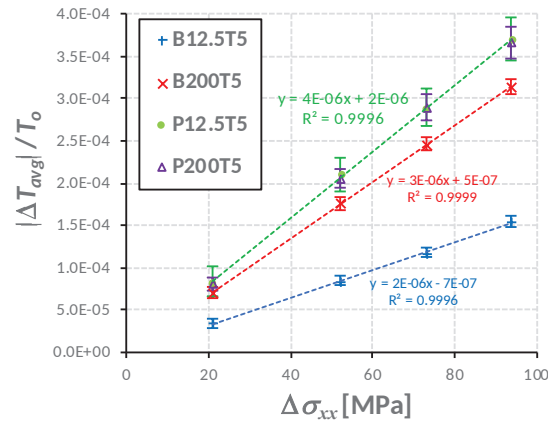

Figure 6: Plots of normalized Thermoelastic Signal versus load amplitude.

4.1 Influence of spectral leakage and frame dropping

Figure 7 shows some examples of the error introduced by spectral leakage with varying number of processed frames. As mentioned in Section 3, the correct amplitude of the thermoelastic signal, ΔT, is obtained when the number of processed frames is such to provide a frequency bin exactly at the load frequency, as this guarantees the averaging of an integer number of load cycles. The error in Figs. 7 is defined as:

$$Leakage\ Err = \frac{\widetilde{\Delta T} - \Delta T}{\Delta T} \times 100 \qquad (8)$$

where ΔT is the correct value, calculated with a number of frames yielding an integer k, and $\widetilde{\Delta T}$ is the actual value with a generic number N of frames.
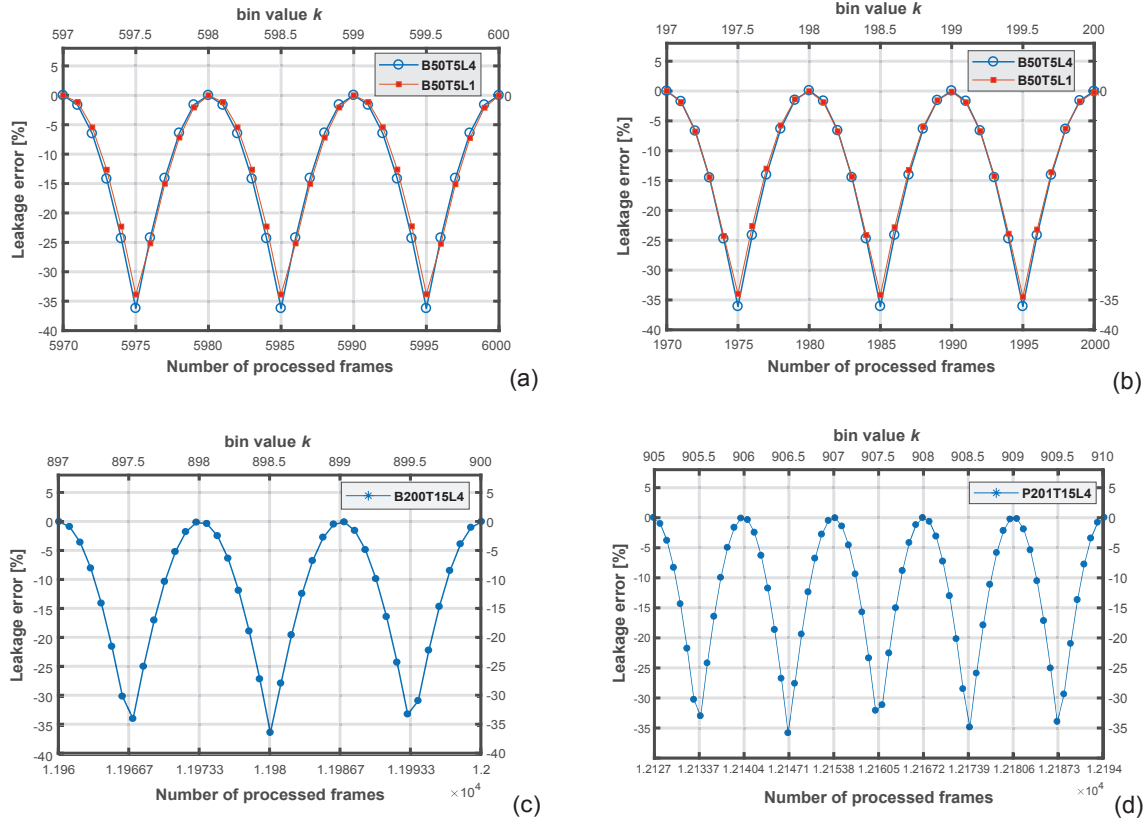

Figure 7: Plots of leakage error versus a range of processed frames and frequency bin values.

Figure 7a shows the error fluctuation for a range of values of N which yields three consecutive integer values of k, from 597 to 600. This first example has a SF=50 Hz and N=6000 corresponds to a TW=120 s. The plot shows that the error has a fluctuation between 0 and about 36 % which is almost identically repeated between two consecutive integer values of k. The same plot shows a comparison between two load amplitudes: the minimum, L1, and the maximum, L4, applied. It is found that the extent of the error is little influenced by the load amplitude. Fig. 7b reports the same error plot but for a smaller number of processed frames, with N=2000 now corresponding to a TW=30 s. It is seen that the error is almost identical to that computed with a longer acquisition. Such comparison was performed with varying TW, and it was observed that also this parameter does not affect the leakage error fluctuation. Figure 7c shows an example of spectral leakage at a higher SF of

200 Hz, but same TW=120 s. It is once again seen that the error fluctuation is similar and still oscillating between 0 % and 36 %. Finally, Fig. 7d reports the error measured from data acquired with the P camera, at a SF=201 Hz and LF=15 Hz (i.e. similar parameters to those in Fig. 7c). It is found that the leakage error is similar also for the P camera.

Evaluations like those reported in Fig. 7 were made for all testing parameters and both cameras, and in conclusion it was always observed a similar behavior for all tests. In particular, the leakage error always determines an attenuation of the thermoelastic signal, which is maximum whenever the number of processed frames is such to include an odd number of half-cycles. Moreover, the leakage error does not depend significantly on the load amplitude, the camera type and the number of sampled cycles N (i.e. the time window TW). Therefore, extending the duration of the acquisition does not provide safety against this type of error. Also, the error fluctuation is cyclic, and the length of each such cycle depends on SF and LF, but in TSA it generally involves a few tens of cycles. The leakage error still needs to be carefully avoided, regardless of type of camera sensor used, as the error can rise as high as about -36%, which is not negligible.

It is reported that the leakage error in signal processing by the Discrete Fourier Transform was also investigated in the work of Thompson and Tree [29], who have indeed shown that an attenuation of 36.34 % is the maximum difference between the real and calculated signal amplitude, due to leakage.

Another source of error is the frame-drop from missed streaming of one or more frames during frame grabbing, as described in Section 3.1. An example is provided in Fig. 8, which shows how such error could become rather large. In particular, Fig. 8a shows the plot of the time interval between two ensuing frames. This information is retrieved from the FlirResearchIRmax software and might not be available with other IR camera systems. The analyzed example has a SF=200 Hz, and therefore the grabbing time interval should be 1/SF=0.005 s. Figure 8a allows to check at a glance all the grabbing history. It is seen that there are three occurrences where the time interval is bigger than 0.005 s: two at a very early stage of acquisition, and a third one after about 2050 frames. This latter is equal to 0.04 s and correspond to 7 frames dropped. Figure 8b shows the thermoelastic signal versus the number of frames used for its evaluation. The frame-drops at N=2050 is in particular responsible for a big change of ΔT, which does not recover with the increasing number of processed frames. The constant value of the curve for the case where frames have been restored, indicates that the procedure described in Section 3.1 (Step 1) is very effective. Figure 8b also shows the value of the standard

deviation calculated over the ROI of the sample. There are no meaningful differences in standard deviation between the two cases of frame-drop and frame-restored, and it is only seen that the standard deviation increases with the reduction of frames analyzed, as should be expected.
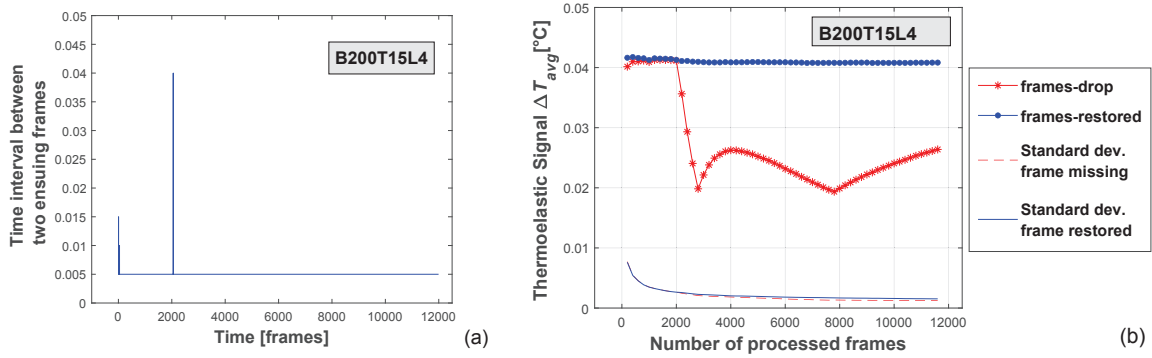

Figure 8: a) Evaluation of frame-drops from acquisition of the time interval between grabbed frames; b) comparison of thermoelastic signal with and without frame-drop at varying N.

4.2   Influence of setup parameters: LF, SF, TW

Values of the average thermoelastic signal, ΔT_{avg}, and standard deviation, St.dev., evaluated over the sample ROI data, have been calculated with varying LF, SF (see Fig. 2) and TW. Figures 9 and 10 show plots of ΔT_{avg} and noise-to-signal ratio, St.dev./ΔT_{avg}, versus TW, expressed both in seconds (Figs. 9b, 10b) and in number of loading cycles (Figs. 9c and 10c). This comparison is here shown only for tests at load amplitude L4, since the general trends observed are not significantly changed by the load amplitude.

First of all, it is noticed that the values of ΔT_{avg} from the P camera (Fig. 9a) are very little influenced by LF, as predicted by the Thermoelastic Law. Therefore, the cooled sensor is able to capture the exact thermoelastic effect induced temperature change. On the contrary, the B camera exhibits an attenuation which increases with LF (Fig. 10a). Both Figs. 9a and 10a also show that the value of ΔT_{avg} is basically constant for TWs above 10 s, i.e. the accuracy is not influenced by TW after a certain number of minimum loading cycles has been acquired. For the case of LF=1 Hz, 10 loading cycles are already able to provide a good estimation of ΔT_{avg}.

A noteworthy result, relative to the P camera, is that SF has a negligible influence on ΔT_{avg}, i.e. also a small number of sampled points per load cycle are able to provide a good average estimation of the thermoelastic signal.

Another important metric is the standard deviation, which provides indications on TSA stress-measurement sensitivity [5]. Contrary to ΔT_{avg}, both TW and SF now have a significant influence on the noise-to-signal ratio,

which increases with decreasing of TW, number of loading cycles and SF (see e.g. Fig. 9b,c 10b,c). In particular, Fig. 10c reveals that the noise-to-signal ratio decreases with the concurrent increase of SF and decrease of LF, i.e. with increasing the number of sampled points per loading cycle. Since the St.dev. is evaluated over a ROI, it also provides an indication of spatial precision of the measurement. As pointed out by Rajic and Street [5], this is further influenced by the different gain and offset responses of each sensor in the focal-plane-array. These determine a Fixed-Pattern-Noise (FPN) that can be only attenuated by an initial, or periodically performed, Non-Uniform-Calibration (NUC). Plots in Fig. 9b,c-10b,c confirm the general trends observed in [5], exhibiting an initial log-linear decrease of the *noise-to-signal* ratio, attained by cross-correlation, which gradually attenuates towards an horizontal asymptotic bound, promoted by the FPN. It is observed that the noise-to-signal values from both the P and B cameras are slightly lower than those reported in [5] under similar setting conditions (LF=5 Hz, SF=50 Hz). This might be due to the better control of stress-field uniformity with the tensile dog-bone sample compared to hole-in-plate sample used in [5], but also to the different materials used in the two works.
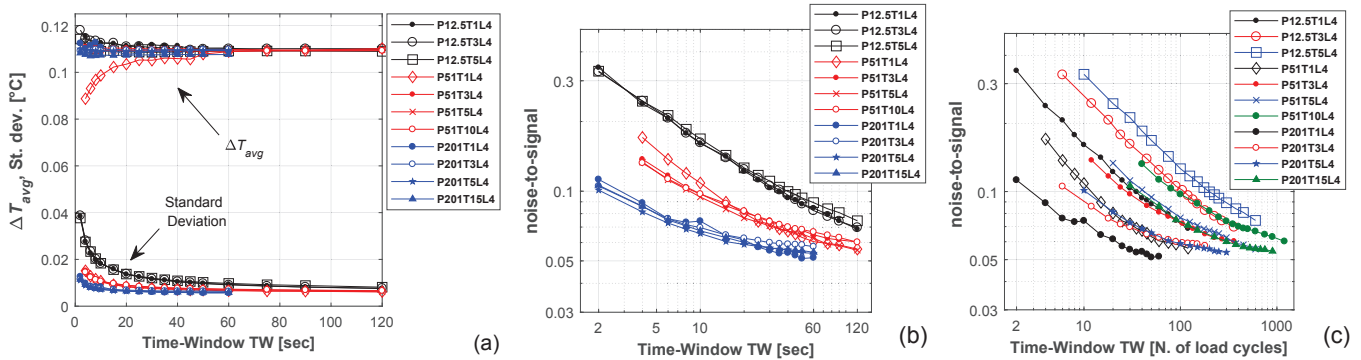

Figure 9: Data from the P camera: a) thermoelastic signal *vs* time-window duration; b) noise-to-signal *vs* time-window duration; c) noise-to-signal *vs* number of loading cycles, at varying LF and SF. The P camera integration time set is 659 µsec.
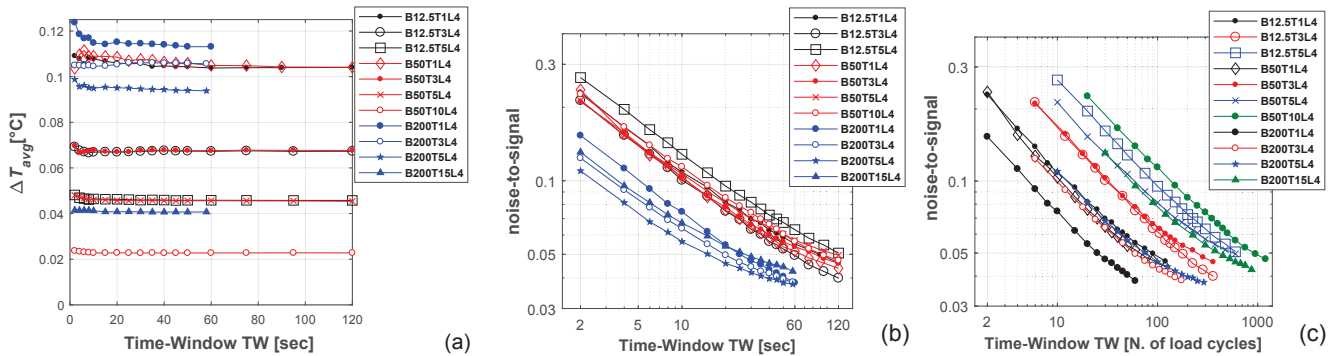

Figure 10: same as Fig. 9. Data from the B camera.

A final consideration arises from Fig. 10. Since the thermoelastic signal amplitude measurement is fairly stable after about 10÷20 s, and since the noise-to-signal ratio does not decrease significantly either for longer runs, extended TWs are in most cases not necessary and possibly to avoid. In fact, acquiring short blocks of data would reduce the risk of frame dropping and drifts in the detector response [21]. This is even more the case for bolometer detectors, which are less stable than photon ones, and where drifts of the FPN are generally avoided by periodic internal NUC calibrations which cannot operate during long TSA acquisitions.

4.3   Thermoelastic constant correction

Figure 10a shows that the attenuation of the thermoelastic signal measured with the B camera at LF=1, 3, 5 Hz, is the same for SF=12.5 Hz and 50 Hz. A similar outcome is obtained in [25], where it was stated that the thermoelastic signal attenuation ratio depends mainly on the loading frequency, and not on SF, load amplitude and material being tested. By recalling Eq. 1, it is possible to define the thermoelastic signal attenuation ratio as follows:

$$\frac{\Delta T}{T_o C_{th} \Delta\left(\sigma_{xx} + \sigma_{yy}\right)} = C_{LF}$$

(9)

where $0 < C_{LF} < 1$. By recalling what written at the beginning of Section 4 about the linearity between ΔT and $\Delta\sigma_{ii}$ and introducing a coefficient $C_B = C_{th} \times C_{LF}$, Eq. (9) can be rearranged yielding:

$$C_B = \left[\frac{\left|\Delta T_{avg}/T_o\right|}{\Delta\sigma_{xx}}\right]_{LF}$$

(10)

where the term within square brackets in Eq. (10) is the slope of the linear regression of ΔT vs $\Delta\sigma_{ii}$ for each value of LF, SF and TW. The coefficient C_B is expected to be a function of LF and can be regarded as a new thermoelastic constant, which can replace the material specific C_{th} in order to retrieve the correct thermoelastic signal.

Figure 11 shows plots of $\ln(C_B/C_{th}) = \ln(C_{LF})$ versus LF, where C_{th} is the material thermoelastic constant obtained from data acquired with the P camera. A different behavior is observed between SF=12.5 and 50 Hz on one side, and SF=200 Hz on the other. In particular, values relative to 12.5 and 50 Hz are found to almost overlap and are well interpolated by the same semi-log linear regression proposed in [25]. On the contrary, the

slope of the interpolation line with SF=200 Hz is different. Quite unexpectedly, the thermoelastic signal attenuation coefficient C_{LF} at 200 Hz is significantly smaller than that for 12.5÷50 Hz.

The different behavior at 200 Hz is most likely to be attributed to the sensor sub-windowing. In fact, it is recalled that the A655sc uses the full-frame array (640×480) for sampling frequencies up to 50 Hz, and a sub-windowed array (640×120) at 200 Hz. It is unclear why this should affect the amplitude response, since the sensor time-constant should be an intrinsic property o the sensor material, which does not depend on the dimensions of the sensor sub-array [21]. It is interesting to recall how sub-windowing affects sensitivity in photonic detectors. In this latter case, a sub-windowed array has a smaller number of data sent to the read-out circuit, and this produces a reduction of data transfer times. This gain in time can be used to set a longer integration time, which ultimately increases the sensor sensitivity. It is then suggested that the increase of the staring time, determined by the smaller amount of data transferred by a sub-windowed array, might explain the sensitivity increase in the A655sc camera at 200 Hz. Of course, this conjecture will need further future investigation. It is observed that previous works using the Flir A655sc or similar systems, [5,21,24,25], have not explored sampling frequencies higher than 50 Hz, or sub-windowing (where allowed), and did not report the sampling frequency as being a potential source of influence in signal attenuation. In light of the results in this work, the influence of SF should be carefully verified and considered.
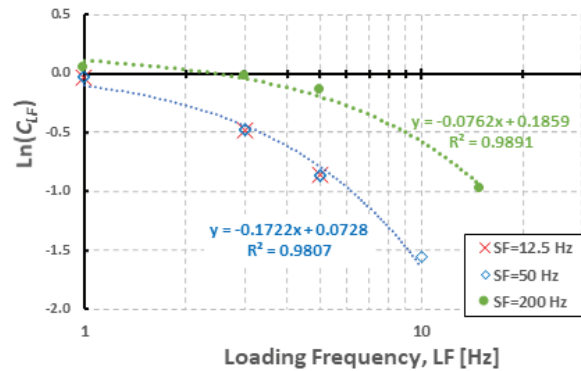

Figure 11: plots of the thermoelastic signal attenuation coefficient, C_{LF}, versus the loading frequency.

5. Results and discussion #2: SENT sample

The bi-axial stress field of the SENT sample allows to evaluate the true TSA signal processing performances, as the signal cannot be further improved by spatial averaging, as done with the tensile coupon. Figure 12 shows

a comparison of full-filed maps of ΔT. Results are shown for a test case with LF=10 Hz and SF=50 Hz, but all the comments below can be extended to all tests and different set parameters.

From Fig. 12 it is observed that the maps acquired with the B camera are able to reproduce the stress distribution features and isopachics patterns. The signal is proportionally attenuated, and therefore the maps are rescaled by a constant factor with respect to the maps acquired from the P camera. Therefore this qualitative comparison confirms the findings from the tensile tests, i.e. that signal attenuation is linearly proportional to the local stress amplitude $\Delta\sigma_{ii}$. On a more practical perspective, this means that TSA performed with low cost micro-bolometers can be exploited to check for damage induced stress concentrations in dynamically loaded structures.

Figure 12 also compares the signal obtained from a long TW=120 s, with a short TW=10 s. It is immediate to notice that the short TW gives rise to a higher spatial noise, but this does not alter the isopachic distribution and signal amplitude.
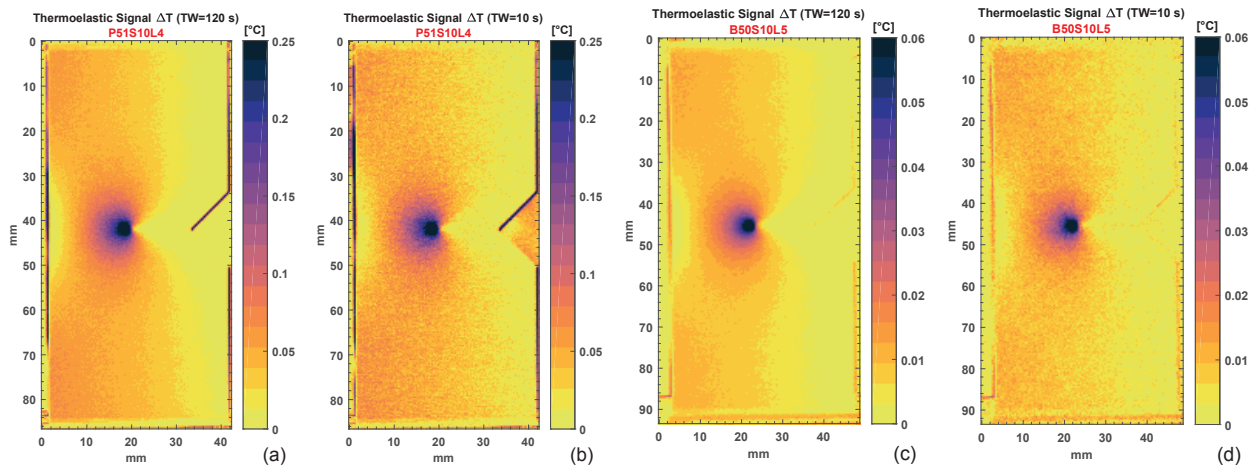

Figure 12: maps of the thermoelastic signal evaluated with the P camera (a, b) and B camera (c, d), and with different TW of 120 s (a, c) and 10 s (b, d).
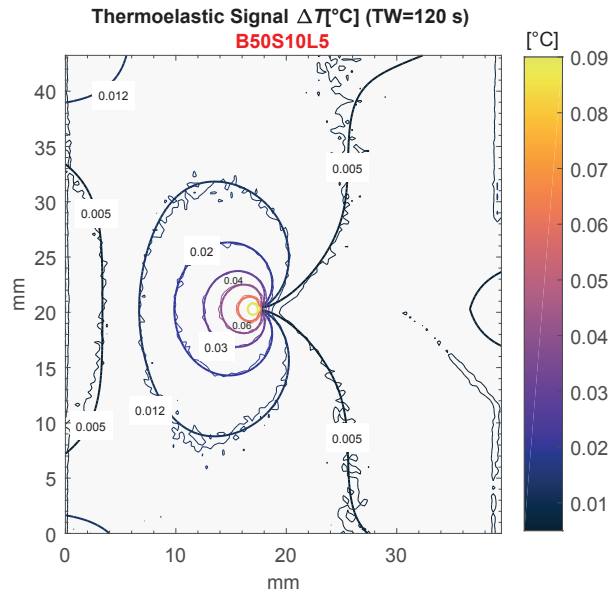
Figure 13: thermoelastic signal map of test B50S10L5: comparison of experimental and analytical (least square fit) contour plots.

As outlined in Section 3.3, the Williams' series expansion model, adapted as in Eq. (9), can be used to fit the isopachics. Since the B sensor influence is reduced to an attenuation of the thermoelastic constant C_{th}, which is replaced by C_B, Eq. (9) should be still formally able to fit the maps of ΔT from the B camera. This is indeed demonstrated in Fig. 13, where the contour plots of the experimental data and the excellent analytical fitting are shown. Since the matching is also very robust, in that it works equally well with other acquisition parameters, it could be used as inverse calibration procedure, i.e. to obtain C_B from a sample with a reproducible and known SIF. The suitability of Eq. (9) to fit B camera maps allows also to run the algorithm evaluating the crack tip, which is as effective as with P camera data. It is here noticed that this algorithm can be applied even if the correct C_B is not known. In this case, i.e. using a wrong value of C_B, the value of the SIF returned by the fitting will be not exact, but the fitting capabilities of the model still would work, yielding the correct estimation for the position of the crack tip. Therefore, the procedure outlined in Section 3.3 could be applied simply for qualitative crack-tip tracking.

Figure 14 shows a comparison of thermoelastic signal phase maps from a strip-area centered along the crack line. The reason for this comparison is to asses if the B-camera is able to catch the typical local phase shift that is formed ahead of the crack tip due to some peculiar material behaviors such as: formation of a plastic zone or heat transfer favored by steep stress gradients [12]. Here it is worth quoting also the work of Rajic and Rowlands [21], who stated that further peculiar phase delay causes could arise in bolometers, e.g. due to the

detection integration process or scan delays between the different detector cells in the array. From Fig. 14 it is possible to conclude that the phase map from the B camera is very similar to that of the P camera, and this is at least so also with varying loading frequency. It is also observed that the phase-shifted area ahead of the crack tip is only slightly bigger with the B camera.
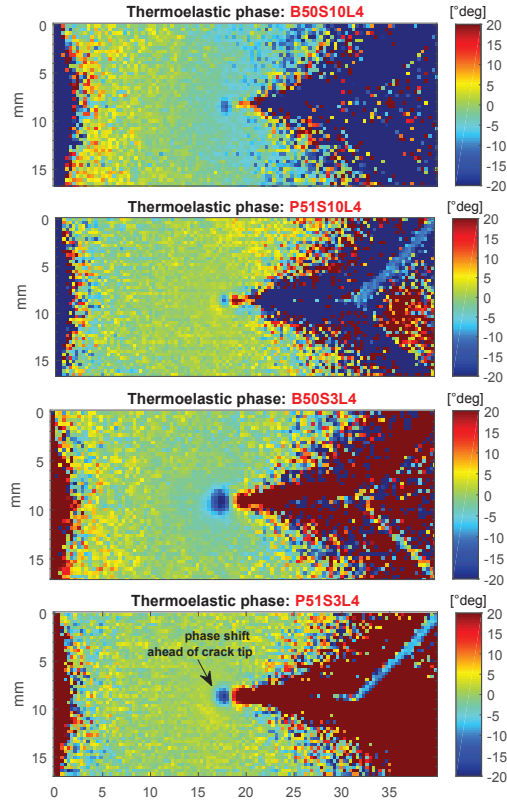

Figure 14: maps of thermoelastic signal phase near the crack tip: comparison between P and B cameras and different loading frequencies of 3 and10 Hz.

5.1   Evaluation of the SIF and bolometer data correction

Figure 15 shows the values of SIF, calculated by least-square fitting of the Williams's model (see Eq. 6), considering a value of the thermoelastic constant C_{th}=3.9×10^{-6} MPa^{-1}, as measured from the tensile tests with the P-camera. It is seen that the SIF value obtained with the P-camera is the higher, while the signal attenuation reduces the SIF in the case of the B-camera, with a reduction that increases with LF and decreases with SF, in a similar manner of ΔT_{avg}, see comments in Sections 4.2 and 4.3.
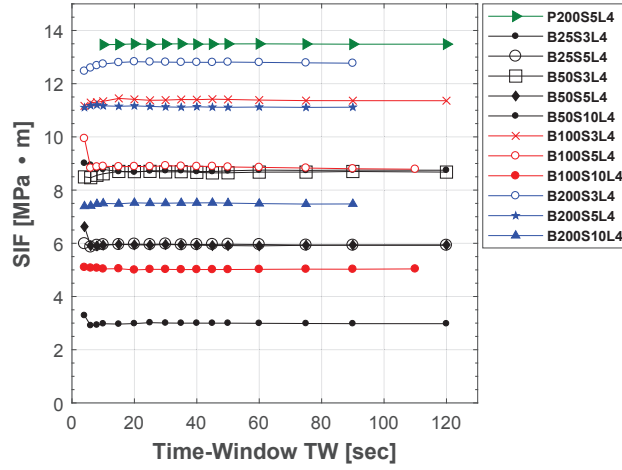
Figure 15: Mode I Stress Intensity Factor *vs* frame grabbing time window, for different LF and SF.

Figure 15 also reports the influence of TW duration, where each block of analyzed frames was optimized to eliminate spectral leakage errors and to correct frame-dropping, when detected. It is remarkable to observe how the value of the SIF is pretty much stable with any values of TW longer than about 10 s. This also means that the Williams' least-square fitting algorithm is able to cope well with the higher noise left by short TW acquisitions (as shown in Fig. 12).

Since the Williams' coefficients in Eq. (9) are linearly correlated to the thermoelastic constant, and this is C_{th} for the P-camera and $C_{th} \times C_{LF}$ for the B-camera, with C_{LF} depending on LF and SF, it is then possible to retrieve the correct value of stress intensity factor, which here is assumed to be the SIF measured with the P-camera, SIF_P, from the SIF calculated with the B-camera, SIF_B. This correction reduces to the simple formula:

$$\left(\Delta K_I\right)_P = \left(\Delta K_I\right)_B \frac{C_{th}}{C_B} = \frac{\Delta K_{IB}}{C_{LF}} \tag{11}$$

Where C_B or C_{LF} are the same thermoelastic constant correction factors calculated from the tensile tests (see Eq. (10)). The following table 1 reports some results of corrected values of SIF using Eq. (11).

Table 1 - Values of the SIF, ΔK_I, in [MPa×m$^{0.5}$]

SF [Hz]	25		50			100			50*	100*	200		
LF [Hz]	3	5	3	5	10	3	5	10	5	5	3	5	10
SIF_P	13.58 ± 0.47											
C_{LF}	0.64	0.44	0.64	0.44	0.17	0.8	0.63	0.37	0.823	0.82	0.96	0.82	0.56
SIF_B	8.72	5.95	8.68	5.93	2.98	11.4	8.87	5.02	11.15	11.12	12.8	11.1	7.51
SIF_B/C_{LF}	**13.7**	**13.6**	**13.6**	**13.5**	**17.4**	**14.3**	**14.1**	**13.7**	**13.55**	**13.51**	**13.4**	**13.5**	**13.4**
error [%]	0.73	0.09	0.21	0.24	28.45	5.10	3.57	0.86	0.22	0.49	1.64	0.40	1.63

From Table 1 it is seen that the values of C_{LF} for SF=25 and 50 Hz are the same, as discussed in Section 4.3. In fact, the array dimension at SF=25 Hz is still 640×480, as for SF=12.5 and 50 Hz. The values of C_{LF} for SF=200 Hz are instead different as predicted by Fig. 11. Table 1 also considers the case of SF=100 Hz, for which the camera array is sub-windowed to 640×240. Since there are no tensile tests performed at SF=100 Hz that could be used for calibrating C_{LF}, and since the detectors array size is different from SF=200 Hz (i.e. 640×120), an interpolation was proposed to derive a value of C_{LF_100} from those experimentally determined of C_{LF_50} and C_{LF_200}. In particular, a linear interpolation is proposed between C_{LF} and the dimensions of the array, which writes:

$$\frac{C_{LF100} - C_{LF50}}{C_{LF200} - C_{LF50}} = \frac{640 \times 240 - 640 \times 480}{640 \times 120 - 640 \times 480} = \frac{2}{3} \rightarrow C_{LF100} = \frac{\left(2C_{LF200} + C_{LF50}\right)}{3} \tag{11}$$

The columns in Table 1 with SF=50* Hz and 100* Hz refer to the case of data acquired with SF=200 Hz and subject to a numerical down-sampling, i.e. considering 1 sample every 4 (SF=50*) and 1 every 2 (SF=100*). This allowed to verify that, since the original array size is always 640×120, the working values of C_{LF_50*} and C_{LF_100*} must be the same as C_{LF_200}, i.e. the dependency of C_{LF} with the sampling frequency SF is generated only by a change in the detectors array size.

The last row in Table 1 reports the mean percent error between SIF_P and the values of corrected SIF, SIF_B/C_{LF}. Apart from one value, all the others fall well within the band of dispersion of SIF_P. It is then possible to conclude that the SIF correction procedure, based on the thermoelastic correction coefficient C_{LF}, is effective and may allow the use of micro-bolometer cameras for quantitative fatigue crack growing characterizations at both material and structure level.

5.2 Crack tip monitoring and computation times

The crack-tip position, as outlined in Section 3.3, is found after searching the optimal fitting of the isopachics' shape with the Williams' functions. The procedure can be performed also on un-calibrated data, and can achieve pixel accuracy. Figure 16a shows an example of crack tip detection. The method was also tested in [12], using the same sample and data from the P-camera, and an excellent agreement was found between the proposed procedure and the location measured by an external optical device. In the present work, it is further reported that the crack-tip position was not influenced by the number of analyzed frames (between 5 and 120

s of TW), and the positions found by the B and P camera differed less than the smaller pixel accuracy. It is also added that the seed point for the search algorithm was automatically established as the point with higher temperature in the central sample region, and a window of 11×11 pixels, centered on the seed point, was adopted as search region.

A final important evaluation in this study regards the computation time and general burden required to perform all the presented analyses. A key role in the proposed low-cost setup is played by the off-line post-processing, which allows to zero the software costs and limit the hardware to the IR-camera only.

All the post-processing in this work was performed in Matlab (see Appendix A), which allows to measure the elapsed time through the tic/toc functions. These have been used to evaluate the computation time of two different scripts:

- *Script 1*: this script performs the optimization of the number of processed frames to minimize spectral leakage, and the cross correlation summation. The input to the script is the load frequency, which is assumed to be the lock-in frequency, the sampling frequency and the thermograms. The output comprises the maps of thermoelastic signal amplitude and phase. An example of such script is reported in Appendix A;

- *Script 2*: this performs the same operations of script 1, and has the same variables in input. It then adds the iterative algorithm which retrieves the optimal crack tip location and the calculation of the SIF.

Figure 16 summarizes the results of the computation time analysis. These have been obtained by running the scripts on a laptop Dell XPS 15 9560, equipped with an Intel i7 - 7700HQ 2.8 GHz processor and with 16 GB RAM DDR4 2400 MT/s. It is also added that *script 1* was applied on a sub-window of 231×115 pixels, corresponding to the whole map shown in Figure 16a. *Script 2* was applied on a sub-window of 90×80 pixels, comprising all the ligament area of the sample in front of the crack tip and part of the wake of the crack (see the green rectangle show in Fig. 16a). Results in Fig. 16b,c refer to the B camera only. The processing time for *script 1* is found to grow linearly with the TW extension. Given the nature of the correlation summation, it is immediate to realize also that the processing time, at given TW, is proportional to the sampling frequency. The steel SENT sample analyzed in this work is already able to provide stable estimations of C_{th}, C_{LF} and SIF with values of TW= 20 s and SF=50 Hz, which require a *script 1* run time of only 0.3 s, which grows to 1.1 s with SF=200 Hz.
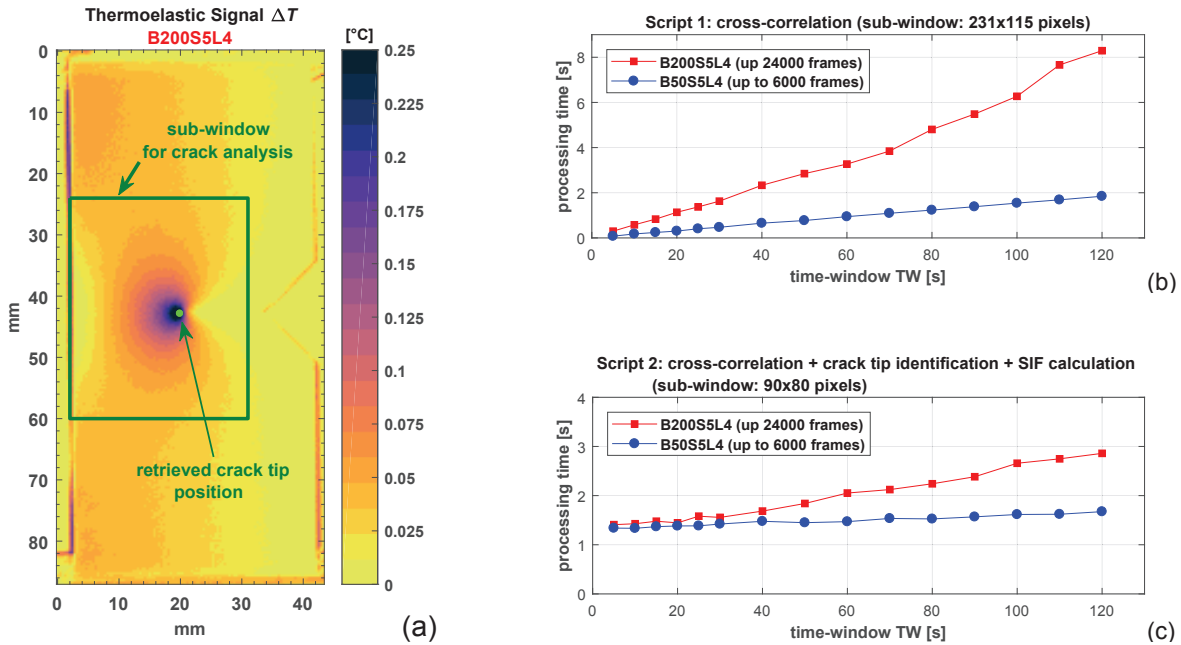
Figure 16: a) Thermoelastic signal map with crack tip identification and sub-window area analyzed by script 2; b,c) examples of processing times for script 1 (b) and 2(c).

Regarding script 2, it is seen that both the evaluations at SF=50, 200 HZ grows linearly with TW, starting from an offset time of about 1.35 s. This initial value basically accounts for the time spent to evaluate the crack tip position and the SIF, while cross-correlation summation is clearly responsible for the increase in time with the increased number of processed frames. It is also observed that the cross-correlation processing time is shorter than *script 1*, because of the smaller sub-window analyzed by *script 2*. It is finally pointed out how a full TSA and crack-tip analysis (including crack tip position and SIF) can be performed in about 1.4 s (at TW=20 s, and SF=50 to 200 Hz). Of course such short time processing requires an appropriate sub-windowing, but if the purpose is to characterize and monitor over time the crack tip behavior, it is not so important to obtain extended maps of the thermoelastic signal at each measuring step. It is also believed that computation times under 2 s would still be compatible for providing feedback loop-control to testing machines during fatigue loading, allowing to run tests under SIF or crack growth rate control [23].

Another key feature of the proposed signal processing is the use of a self-reference signal, i.e. the frequency of the harmonic signal used in the cross-correlation is not obtained by physically sampling the load signal [31]. This allows to save in hardware setup, as no IR camera with specific lock-in ingress or supplementary hardware is needed to synchronize, sample and mix the load signal. As mentioned in Section 3.1 (STEP 2), the lock-in frequency can be extracted with a preliminary DFT analysis of a single pixel or averaged area signal, ensuring

that the spectral leakage is opportunely kept low. In the present work, this procedure was done in all tests, and it was consistently found that every time that the self-reference lock-in frequency coincided with the nominal value of the load frequency set in the testing machine. The self-reference frequency extraction algorithm was not included in the scripts time testing in Fig. 16. It was verified, though, that the procedure can be automatized (no external manual input required) and it takes only a few tenths of seconds to run, therefore it does not undermine the considerations made above.

It is finally observed that in commercial TSA systems, where in-line analysis is presented as a plus feature and sold as a real-time analysis, a prominent portion of the overall analysis time is spent to acquire a sufficient number of frames [21]. The figures in Fig. 16b,c show that in off-line analyses the extra time added to this unavoidable data collection time is of the order of few seconds, and this could be still shortened if IR camera suppliers would implement the required signal processing in their native IR camera control softwares. As demonstrated by the algorithm reported in Appendix A, at least for cross-correlation only, adding such feature should be trivial. Alternatively, allowing to save the thermograms in .mat Matlab format, rather than ASCII text format, would be enough for anybody to run their own analyses with little time spent in preparing the input data.

6. Conclusions

A low cost experimental setup has been evaluated, able to implement Thermoelastic Stress Analysis for quantitative evaluations by means of a micro-bolometer IR-detector. The proposed setup requires only one ordinary micro-bolometer and no further hardware devices, while the signal processing is implemented off-line by in-house developed Matlab scripts.

The experimental setup has been verified by testing a tensile and a SENT specimen made of stainless steel 304L, and by simultaneously using a state-of-the-art Photon detector camera to provide a reference thermoelastic signal performance.

Regarding the signal processing developed to evaluate the thermoelastic signal, this implements a cross-correlation procedure coupled with a self-reference signal. In particular, the following novelties and conclusions can be pointed out:

- The thermoelastic signal frequency, needed to build the self-reference signal, can be retrieved by performing a Discrete Fourier Transform spectrum analysis on one point or an average signal from an area. The DFT spectrum is very useful to reveal at a glance: the whole frequency content of the signal, the presence of spectral leakage at the thermoelastic frequency, the extent of flat noise affecting the single pixel signal. To retrieve the thermoelastic frequency, leakage must be dealt with and reduced, and this can be done by modifying the number of processed samples until the cusp at the bin frequency of the thermoelastic signal becomes a single peak;

- The general influence of spectral leakage on the measured thermoelastic signal has been quantified, and it is found that it can generate errors as high as 36 %, which do not depend on the number of thermograms processed but rather on the fraction part of loading cycles acquired. A simple procedure is provided to reduce such error when the thermoelastic frequency is known;

- The loss of a minimum amount of frames during the data streaming to the PC is already able to disrupts the temporal continuity, and give rise to significant errors. A hint of frame-drop error is given when the cusp in the DFT spectrum is not eliminated by setting an integer number of load cycles. The present work has proposed a procedure to correct the loss of frames, which though relies on the ability of the IR camera software to provide the time-base of sampled data;

- A simple cross-correlation script is proposed which provides the thermoelastic signal amplitude and phase maps with processing times that increase linearly with the number of pixels per frame and frames processed. The processing time is generally under 2 s for typical TSA settings.

Regarding the performance of the bolometer camera, this was quantitatively evaluated against the photon detector, by analysing the following parameters: single-pixel and average thermoelastic signal, ΔT and ΔT_{avg}, spatial noise-to-signal ratio, thermoelastic constant C_{th}, thermoelastic bolometer correction factor C_{LF}, and SIF. The influence of setup parameters is in particular analysed, comprising: the loading frequency, the sampling frequency, the acquisition time interval. The following conclusions can be pointed out:

- The linearity between stress change and acquired temperature change, as expected by the first order thermoelastic law, is observed also with the temperature values measured by the bolometer. Such temperature values are, though, reduced by a factor that primarily depends on the loading frequency

(as pointed out in [21,25]). A dependency with array sub-windowing has also been observed for the camera model used in this work, which requires further investigations to fully understand the causes;

- As proposed in [25], the correct thermoelastic signal amplitude from the bolometer can be retrieved by applying a linear coefficient C_{LF}, whose dependency with the loading frequency is well modelled by a semi-log linear regression law. This camera-specific calibration procedure has the potential to allow bolometers to perform quantitative analyses;

- In general, the bolometer exhibits a noise to signal ratio that is comparable, if not better, with that of the photon detector, generally confirming the behaviour observed and commented in [5,21]. While the signal to noise ratio, and therefore TSA sensitivity, improves with the number of acquired loading cycles, or with increasing the sampling frequency and the acquisition time window, the amplitudes of ΔT_{avg} and SIF remains pretty much constant with acquisition time windows above 20 s. This behaviour was observed with all tested sampling frequencies in the range 12.5 and 200 Hz.

Regarding the SENT specimen crack characterisation, the following novelties and conclusions can be pointed out:

- An over-deterministic least square fitting of the Williams' series function is implemented to evaluate the SIF. An automatic implementation in Matlab has allowed to apply the procedure iteratively to search the optimum crack tip position by maximising the R^2 statistical parameter. This crack tip identification procedure relies on the ability of Williams' model to fit the isopachics shape and does not require a thermoelastic or thermographic calibration. Therefore it can be proposed as a general crack-tip tracking procedure;

- The values of the SIF calculated with the bolometer can be directly corrected by dividing for the calibration coefficient C_{LF} (see Eq. (11)). The corrected values of the bolometer's SIFs have been found to be in good agreement with the SIF values calculated with the photon detector;

- The Matlab script implementing cross-correlation, crack-tip identification and SIF evaluation requires processing times under 2 s if the analysed area is limited to a maximum of 200×200 pixels, which is generally enough for full crack characterisation. The proposed Matlab script can be easily extend to include also a 2nd harmonic analysis, which has been found useful to investigate the onset of crack

closure [12] and as a monitoring parameter for detecting damage and early fatigue life limit estimations [6,9].

In summary, the potential use of bolometers for qualitative and quantitative TSA and thermographic structural investigations has been further demonstrated. The setup presented here requires an investment cost limited to the bolometer camera only, i.e. reasonably under 10 K€. Several recent works, including the present, have demonstrated how such equipment and the TSA technique can be used to fully characterise the fatigue behaviour of composites [6,7,15,32] as well as metallic materials under small scale yielding [9,13,22,33,34].

Acknowledgments

Appendix A

A concise example of Matlab script is reported here, which includes the essential steps required to evaluate the thermoelastic signal amplitude and phase from a number of sampled frames. The script is suitable for analyzing structures subject to cyclic mono-frequency loadings.

The input variables in the script are the following:

- `frames` – is a third order tensor of size (n×m×t) which contains all acquired and piled-up thermograms, in either calibrated or un-calibrated units. With reference to the scheme in Fig. A1, n×m are the dimensions in pixels of the single frame. The third dimension, *t*, is time, codified in discrete format, i.e. as the number of frames, `N`;

- `LF` – is the loading frequency in [Hz];

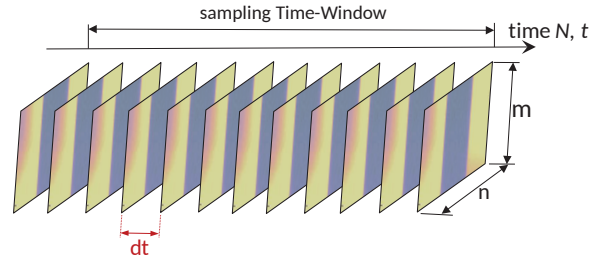- `SF` – is the sampling frequency in [Hz].

Figure A1: scheme of acquired frames, piled-up to form a third order (n×m×t) tensor, named "`frames`".

The Matlab script reads:

```
1.   N=size(frames,3);
2.   k=LF*N/SF;
3.   while rem(k,1)~=0
4.       N=N-1;
5.       k=LF*N/SF;
6.   end
7.   dt=1/SF;
8.   TW=N*dt;
9.   t=0:dt:TW-dt;
10.  X=(2/N)*sum(frames.*reshape(cos(2*pi*LF*t),1,1,numel(t)),3);
11.  Y=(2/N)*sum(frames.*reshape(sin(2*pi*LF*t),1,1,numel(t)),3);
12.  Amp=2*sqrt(X.^2+Y.^2);
13.  Phase=atan2(Y,X)*(180/pi);
```

Lines from 2 to 6 perform an optimization of the number of frames that are subsequently processed by cross-correlation, performed in lines 10 and 11. This preliminary step allows the spectral leakage error to be minimized, and consists of providing a bin in the frequency domain that falls exactly upon the value of LF. If this is not possible to obtain, the spectral leakage can still be minimized by making sure that `rem(k,1)` in line 3 becomes conveniently small. Lines 10 to 12 implement Eqs. (4,5). Variables `X` and `Y` in lines 10 and 11 provide the in phase and in quadrature components of the thermoelastic signal amplitude, while `Amp` in line 12 provides the peak-to-peak variation.

The above script implements a numerical cross-correlation between the infrared signal and a pure harmonic signal at the load frequency (for more details see also [4]). There are alternative lock-in correlation schemes available, based in particular on the Discrete Fourier Transform or on least-square fitting [26]. These more advanced data-processing procedures would generally prove more efficient in analysing the whole frequency content of the acquired signal (see e.g. Section 3.1), but are substantially equivalent to the above digital cross-correlation scheme in terms of numerical performances, yielding the same measurement accuracy and sensitivity [26]. One merit of the script proposed here is that it is very simple, does not require complex

mathematical operations and therefore can be easily translated into many other programming languages. For instance, translation into open source codes, such as Python or the Matlab similar GNU Octave, is trivial. The reported script can analyse datasets acquired by any IR camera, provided that these are made available in ASCII text format. If the dataset is not radiometrically calibrated, the resulting thermoelastic map will be also un-calibrated, but still meaningful in qualitative terms.

All results presented in this work have been obtained with the same script reported here, although this was extended including a DFT based algorithm, able to extract the load frequency LF from the acquired thermograms (self-reference signal) and to analyse the whole frequency content (see e.g. Fig. 3) . The code was also extended with an algorithm for checking and correcting the presence of frame-drops, and algorithms for the evaluation of the SIF with the least square fitting of Williams' model (see Section 5.2 for more info about computation times).

References

[1]   Pitarresi G, Patterson EA. A review of the general theory of thermoelastic stress analysis. J Strain Anal Eng Des 2003;38:405–17. doi:10.1243/03093240360713469.

[2]   Greene RJ, Patterson EA, Rowlands RE. Thermoelastic stress analysis. Springer Handb. Exp. solid Mech., Springer; 2008, p. 743–68.

[3]   Dulieu-Barton JM. Introduction to thermoelastic stress analysis. Strain 1999;35:35–9. doi:10.1111/j.1475-1305.1999.tb01123.x.

[4]   Pitarresi G. Lock-In Signal Post-Processing Techniques in Infra-Red Thermography for Materials Structural Evaluation. Exp Mech 2015;55:667–80. doi:10.1007/s11340-013-9827-1.

[5]   Rajic N, Street N. A performance comparison between cooled and uncooled infrared detectors for thermoelastic stress analysis. Quant Infrared Thermogr J 2014;11:207–21. doi:10.1080/17686733.2014.962835.

[6]   Colombo C, Vergani L, Burman M. Static and fatigue characterisation of new basalt fibre reinforced composites. Compos Struct 2012;94:1165–74. doi:10.1016/j.compstruct.2011.10.007.

[7]   Palumbo D, De Finis R, Demelio GP, Galietti U. Study of damage evolution in composite materials based on the Thermoelastic Phase Analysis (TPA) method. Compos Part B Eng 2017;117:49–60.

doi:10.1016/J.COMPOSITESB.2017.02.040.

[8]   Shiozawa D, Inagawa T, Washio T, Sakagami T. Accuracy improvement in dissipated energy

         measurement by using phase information. Meas Sci Technol 2017;28:044004. doi:10.1088/1361-

         6501/28/4/044004.

[9]   Colombo C, Vergani L. Thermographic applications for the rapid estimation of fatigue limit. Procedia

         Struct Integr 2019;24:658–66. doi:10.1016/J.PROSTR.2020.02.058.

[10]   De Finis R, Palumbo D, Ancona F, Galietti U. Fatigue limit evaluation of various martensitic

         stainless steels with new robust thermographic data analysis. Int J Fatigue 2015;74:88–96.

         doi:10.1016/j.ijfatigue.2014.12.010.

[11]   Meneghetti G, Ricotta M, Pitarresi G. Infrared thermography-based evaluation of the elastic-plastic J-

         integral to correlate fatigue crack growth data of a stainless steel. Int J Fatigue 2019;125:149–60.

         doi:10.1016/j.ijfatigue.2019.03.034.

[12]   Pitarresi G, Ricotta M, Meneghetti G. Investigation of the crack tip stress field in a stainless steel

         SENT specimen by means of thermoelastic stress analysis. Procedia Struct. Integr., vol. 18, Elsevier;

         2019, p. 330–46. doi:10.1016/j.prostr.2019.08.173.

[13]   Sakagami T, Izumi Y, Shiozawa D, Fujimoto T, Mizokami Y, Hanai T. Nondestructive Evaluation of

         Fatigue Cracks in Steel Bridges Based on Thermoelastic Stress Measurement. Procedia Struct Integr

         2016;2:2132–9. doi:10.1016/j.prostr.2016.06.267.

[14]   Rajic N, Brooks C. Automated Crack Detection and Crack Growth Rate Measurement Using

         Thermoelasticity. Procedia Eng 2017;188:463–70. doi:10.1016/j.proeng.2017.04.509.

[15]   Pitarresi G, Scalici T, Catalanotti G. Infrared Thermography assisted evaluation of static and fatigue

         Mode II fracture toughness in FRP composites. Compos Struct 2019;226:111220.

         doi:10.1016/J.COMPSTRUCT.2019.111220.

[16]   Chase SB, Adu-Gyamfi Y. Evaluation of Fatigue-Prone Details Using a Low-Cost Thermoelastic

         Stress Analysis System. FHWA/VTRC 17-R8,

         Http://WwwVirginiadotOrg/Vtrc/Main/Online_reports/Pdf/17-R8Pdf 2016:53p.

[17]   Weihrauch M, Middleton C, Greene R, Patterson E. Low-Cost Thermoelastic Stress Analysis. In:

         Baldi A, Kramer SLB, Pierron F, Considine J, Bossuyt S, Hoefnagels J, editors. Residual Stress.

Thermomechanics Infrared Imaging Inverse Probl. Vol. 6, Cham: Springer International Publishing; 2020, p. 15–9.

[18] Audenino AL, Crupi V, Zanetti EM. Thermoelastic and elastoplastic effects measured by means of a standard thermocamera. Exp Tech 2004;28:23–8. doi:10.1111/j.1747-1567.2004.tb00155.x.

[19] Pitarresi G, D'Acquisto L, Siddiolo AM. Thermoelastic stress analysis by means of an infrared scanner and a two-dimensional fast Fourier transform-based lock-in technique. J Strain Anal Eng Des 2008;43:493–506. doi:10.1243/03093247JSA348.

[20] Zanetti EM, Musso SS, Audenino AL. Thermoelastic Stress Analysis by means of a standard thermocamera. Exp Tech 2007;31:42–50. doi:10.1111/j.1747-1567.2007.00147.x.

[21] Rajic N, Rowlands D. Thermoelastic stress analysis with a compact low-cost microbolometer system. Quant Infrared Thermogr J 2013;10:135–58. doi:10.1080/17686733.2013.800688.

[22] Rajic N, McSwiggen D, McDonald M, Whiteley D. In situ thermoelastic stress analysis–an improved approach to airframe structural model validation. Quant Infrared Thermogr J 2018;00:1–27. doi:10.1080/17686733.2018.1497898.

[23] Thatcher JE, Crump DA, Devivier C, Bailey PBS, Dulieu-Barton JM. Low cost infrared thermography for automated crack monitoring in fatigue testing. Opt Lasers Eng 2020;126:105914. doi:10.1016/j.optlaseng.2019.105914.

[24] Jiménez-Fortunato I, Bull DJ, Dulieu-Barton JM, Thomsen OT. Towards integrating imaging techniques to assess manufacturing features and in-service damage in composite components. Conf. Proc. Soc. Exp. Mech. Ser., vol. 7, 2019, p. 97–100. doi:10.1007/978-3-319-95074-7_18.

[25] Jiménez-Fortunato I, Bull DJ, Dulieu-Barton JM, Thomsen OT. Towards developing a calibration technique to apply TSA with micro-bolometers. BSSM 13th Int. Conf. Adv. Exp. Mech., 2018, p. 10–1.

[26] Pitarresi G. Evaluation of lock-in signal data processing procedures for Thermoelastic Stress Analysis. BSSM 14th Int. Conf. Adv. Exp. Mech. , 9th -11th Sept. 2019, Belfast, 2019.

[27] Urbanek R, Bär J. Evaluation of the Thermo-Elastic Behavior of a High-alloyed Steel by Fourier Transformation based Lock-In-Thermography. Proc. QIRT 2018, 14th Quant. InfraRed Thermogr. Conf. 25 – 29 June 2018, Berlin, Ger., 2018, p. 941–50. doi:10.21611/qirt.2018.127.

[28] Urbanek R, Bär J. Influence of motion compensation on lock-In thermographic investigations of fatigue crack propagation. Eng Fract Mech 2017;183:13–25. doi:10.1016/j.engfracmech.2017.03.043.

[29] Thompson JK, Tree DR. Leakage error in Fast Fourier analysis. J Sound Vib 1980;71:531–44. doi:10.1016/0022-460X(80)90725-7.

[30] Galietti U, Modugno D, Spagnolo L. A novel signal processing method for TSA applications. Meas Sci Technol 2005;16:2251–60. doi:10.1088/0957-0233/16/11/017.

[31] Boyce BR, Lesniak JR. Thermoelastic measurement techniques enabled by self-reference. Conf Proc Soc Exp Mech Ser 2019;7:125–7. doi:10.1007/978-3-319-95074-7_24.

[32] Pitarresi G, Galietti U. A quantitative analysis of the thermoelastic effect in CFRP composite materials. Strain 2010;46. doi:10.1111/j.1475-1305.2009.00660.x.

[33] Meneghetti G, Ricotta M, Pitarresi G. Infrared thermography-based evaluation of the elastic-plastic J-integral to correlate fatigue crack growth data of a stainless steel. Int J Fatigue 2019;125:149–60. doi:10.1016/j.ijfatigue.2019.03.034.

[34] Chen D, Sun S, Dulieu-Barton JM, Li Q, Wang W. Crack growth analysis in welded and non-welded T-joints based on lock-in digital image correlation and thermoelastic stress analysis. Int J Fatigue 2018;110:172–85. doi:10.1016/j.ijfatigue.2018.01.020.